IEEE Access
Multidisciplinary | Rapid Review | Open Access Journal

Received 15 July 2023, accepted 7 August 2023, date of publication 10 August 2023, date of current version 30 August 2023.

Digital Object Identifier 10.1109/ACCESS.2023.3304005

RESEARCH ARTICLE

NL3DLogTNN: An Effective Hyperspectral Image Denoising Method Combined Non-Local Self-Similarity and Low-Fibered-Rank Regularization

HAORAN LIU[1], TIANYU SU[2], XINZHE DU[3], YUXIN ZHAI[4], AND JIANLI ZHAO[2]
[1]College of Mechanical and Electronic, Shandong University of Science and Technology, Qingdao 266590, China
[2]College of Computer Science and Engineering, Shandong University of Science and Technology, Qingdao 266590, China
[3]College of Electrical Engineering and Automation, Shandong University of Science and Technology, Qingdao 266590, China
[4]College of Transportation, Shandong University of Science and Technology, Qingdao 266590, China

Corresponding author: Jianli Zhao (jlzhao@sdust.edu.cn)

This work was supported by the Shandong Provincial Natural Science Foundation Major Program under Grant ZR2021MF104 and Grant ZR2021MF113.

ABSTRACT Hyperspectral image denoising is an important research topic in the field of remote sensing image processing. Recently, methods based on non-local low-rank tensor approximation have gained widespread attention towing to their ability to fully exploit non-local self-similarity. However, existing non-local low-rank tensor approximation methods fall short in capturing the correlations between various modes in hyperspectral images, thus failing to achieve the optimal approximation. To solve this issue, a novel three-directional log-based tensor nuclear norm (3DLogTNN)–based non-local hyperspectral image denoising model NL3DLogTNN is proposed. The correlation between the various modes of the model was obtained by performing TNN decomposition in three directions on the extracted non-local comparable blocks, better capturing the global low-rank property of the image. To effectively solve the proposed NL3DLogTNN model, we developed an approximate alternating direction method of multipliers (ADMM)-based methodology and offered a thorough numerical convergence proof. Extensive experiments are conducted on hyperspectral image datasets with simulated noise and real-world noise, which demonstrated that the proposed NL3DLogTNN model outperforms state-of-the-art methods in terms of quantitative and visual performance evaluation.

INDEX TERMS Hyperspectral image denoising, non-local self-similarity, 3DLogTNN decomposition.

I. INTRODUCTION

Hyperspectral remote sensing images possess abundant spectral-spatial information and demonstrate high spatial resolution, playing a substantial role in ''mineral detection'' [1], ''precision agriculture'' [2], ''urban planning'' [3], environmental monitoring, management and supervision. However, extrinsic factors, including atmospheric absorption of reflected signals, equipment vibration during transmission, incorrect data conversion, and sensor failures will inevitably impact the acquisition and subsequent processing of hyperspectral remote sensing images. Hyperspectral images are prone to pixel damage and a range of noise pollutants, including Gaussian and impulse noise, which are typically distributed across various bands and pixels. Deadline noise and stripes appear occasionally in the adjacent spectral bands. These problems ultimately cause significant degradation of the visual quality of hyperspectral images, adversely affecting the precise extraction of ground object information. Consequently, subsequent operations, such as hyperspectral image unmixing [4], [5], [6], classification [7], [8], [9] and fusion [10], [11]. These factors pose challenges for removing

The associate editor coordinating the review of this manuscript and approving it for publication was Qingli Li.

noise from hyperspectral images are also greatly impacted. These factors pose challenges for removing noise from hyperspectral images. Hence, researchers have proposed a series of denoising algorithms to solve the degradation of hyperspectral images. These denoising algorithms can be classified based on how they process data into denoising algorithms that convert hyperspectral images into two-dimensional matrix data, and those based on tensor algebra models.

Researchers have proposed a series of denoising algorithms mainly model-based and deep learning-based, to remove noise from hyperspectral images.

Methods based on network learning have accomplished the end-to-end restoration of hyperspectral images, allowing the learning of discrepancies between different structures in the images. These methods implicitly model the prior information of hyperspectral images within the network. For example, the HSI-DeNet model [38] is based on dilated convolutions and residual learning; the HSID-CNN model [43] that exploits the correlation between a certain spectral band and its neighbouring bands; and the 3-D QRNN model [44] that employs 3D convolutions to extract both spectral-spatial correlation and global spectral correlation in hyperspectral images. However, network-based methods require a large amount of hyperspectral data for training and also exhibit limited generalisation ability compared to model-based methods, often being able to handle only a single task.

Model-based methods can be classified based on data processing: denoising algorithms that convert hyperspectral images into two-dimensional matrix data [12] and denoising algorithms based on tensor algebra models.

Denoising algorithms for hyperspectral images [12] treat hyperspectral data as a collection of two-dimensional images stacked together based on two-dimensional matrix data and eliminate noise from the hyperspectral image data by processing each band or pixel. For example, Yang et al. [13] viewed hyperspectral data as matrix image blocks with various bands. First, they used sparse coding and local redundant correlation in the spectral domain to model the global redundant correlation within the spatial scope. Subsequently, sparse coding and compressed representation techniques were employed to eliminate noise from the images. Zhang et al. [14] proposed a low-rank matrix restoration model called LRMR for hyperspectral image denoising. To enhance the performance of this model, different non-relief low-rank approximation functions [15] were introduced to investigate the low rankness of flat matrices with hyperspectral images. He et al. [16] further integrated a unified framework that simultaneously considered spectral and spatial low rankness. This was accomplished by employing the nuclear norm to exploit the low-rank structure and total variation regularisation to capture the hyperspectral images' spectral smoothing information.

However, matrix-based methods compel high-dimensional hyperspectral images to be flattened into a two-dimensional structure, destroying the spatial-spectral correlation of hyperspectral images and making it impossible to achieve better denoising performance. It is crucial to consider both spatial and spectral features for effective noise cancellation to maintain the inherent structure of hyperspectral images more effectively. Recently, researchers have examined denoising algorithms based on tensor decomposition models. These denoising algorithms view hyperspectral images as a whole and directly explore them using multi-dimensional linear tensor algebraic decomposition models. Tucker decomposition [17], [18], [19], [20], [21] and CP decomposition [22] were the most commonly used models for denoising. Prominent methods based on CP decomposition include Multi-Layer Sparse Tensor Decomposition (MLSTD) [39], among other notable approaches. Meanwhile, tensor tubal rank defined by tensor singular value decomposition (t-SVD) has demonstrated promising results in LRTA, including tensor completion [23], [24] and tensor robust principal component analysis (TRPCA) [25], [26] and multi-modal core tensor factorisation methods based on Tucker decomposition and t-SVD [40]. Fan et al. [27] denoising model based on low-tubal-rank tensor recovery addresses mixed noise in HSI. Chang et al. [37] proposed a Weighted Low-Rank Tensor Recovery model, integrating the efforts of low-level HSI recovery tasks into a unified framework to fully exploit the structural spectral-spatial correlations in three-dimensional HSI.

However, the aforementioned methods directly consider the global correlation and discard the redundancy of locally repeated patches in the spatial patterns of HSI, i.e., non-local self-similarity (NSS) [28].To maximise the exploitation of prior NSS in noise reduction, numerous non-local-based noise reduction methods [28], [29], [30], [31], [32], [33] have been proposed. Non-local-based methods attempt to divide images into overlapping patches and group similar patches. The differences between local and non-local correlations were considered in [41], and a sparse modelling scheme that fully exploits these two various types of correlations was proposed. An optimal low-rank tensor model was proposed in [42], combining the spectral and non-local induced low-rank models. Peng et al. [28] first proposed a tensor dictionary learning (TDL) method to deal with non-local similar groups, but its robustness was poor. Many state-of-the-art HSI denoising methods based on the TDL architecture have been proposed, including the inherent tensor sparsity (ITS) measure approach [29], [32] and the Laplacian-regularised one-way low-rank tensor recovery problem (LLRT) [30]. However, the ITS approach has reduced flexibility because of the exponentially increasing number of parameters (variables) as the tensor dimension increases, which makes the denoising process challenging. Furthermore, CP decomposition can yield satisfactory results only under relatively large ranks, and the ITS approach cannot sufficiently preserve the correlation between non-local patterns. The correlation between the global spectra and local space cannot be captured by LLRT, despite being an effective method, since it only assumes a low rank under non-local patterns. He et al. [31]

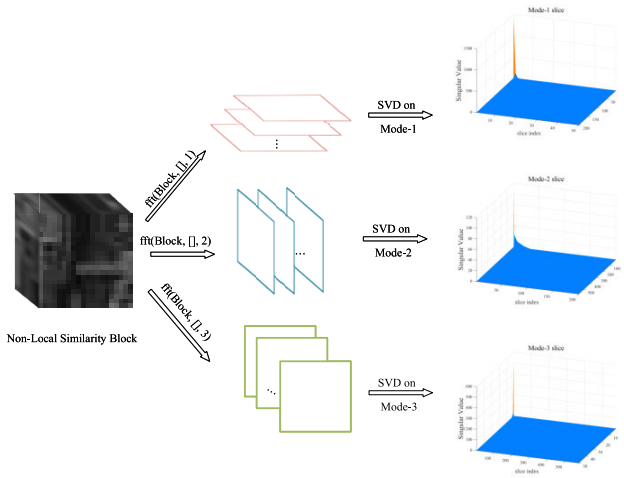

FIGURE 1. Illustration of low-rank prior of the reconstructed non-local similarity blocks in HIS Washington DC Mall.

showed that balancing the correlation between the spectra and NSS can enhance denoising performance. The performance of HSI denoising can still be significantly improved by identifying a tensor representation method, balancing the correlation between all modes, and improving the effectiveness of previous non-local-based methods.

Recently, a novel tensor representation method called 3DLogTNN has been proposed [26]. It extends t-SVD to the k-t-SVD mode and simultaneously removes tension in three directions, making the HSI's low-rank display more flexible and precise. Furthermore, it introduces convex and non-convex three-way logarithmic TNN to further extend TNN, and 3DTNN and 3DLogTNN as their convex and non-convex relaxations, respectively. The 3DLogTNN model has been widely employed in hyperspectral image denoising and outperforms other tensor-decomposition-based denoising models by efficiently eliminating mixed noise while preserving important information.

In this study, the proposed denoising model is based on non-local 3DLogTNN decomposition, which is inspired by the superior effectiveness of the 3DLogTNN representation. A better balance between capturing the worldwide spectral coherence and non-local self-resemblance present in HSI can be achieved via application of 3DLogTNN decomposition for the representation of non-local tensors. Existing high-spectral-image denoising algorithms primarily deal with a single type of noise. However, a real HSI is often subject to the mixed interference of numerous types of noise. Therefore, this study aims to examine HSI denoising algorithms that employ non-local tensor decomposition for heterogeneous noise.

A. MOTIVATIONS AND CONTRIBUTIONS

This article primarily makes two contributions: First, we propose a novel denoising model called NL3DLogTNN that is based on the concepts of non-local self-resemblance and three-mode tensor decomposition, to efficiently eliminate mixed noise from hyperspectral images. The proposed model has two primary advantages. On the one hand, non-local patch processing operations are conducted on hyperspectral images to investigate their global similarity and repetitive patterns. On the other hand, tensor-decomposition-based on t-SVD is conducted individually along each mode when dealing with tensors that have undergone non-local block operations. The multi-mode low-rank features of tensor non-local blocks are effectively captured using the flexible and accurate HSI representation capabilities of 3DLogTNN. Figure 1 shows the HSI Washington DC Mall as an example, we observe that the reconstructed patches under all modes of the non-local similarity block approximation exhibit low-rank behaviour. This shows that both quantitatively and visually, spatial and spectral correlations as well as NSS can be considerably observed.

Second, we develop an approximate alternating direction method of multipliers (ADMM)-based methodology as the solver for the NL3DLogTNN model. In this study, the experimental results on simulated and real datasets demonstrate that the proposed NL3DLogTNN method surpasses related non-local methods for denoising high-dimensional images.

B. ORGANISATION

This article is organised as follows. Section II provides an overview of the notation and framework for HSI denoising. Section III describes the proposed NL3DLogTNN decomposition and its optimisation method. Section IV presents the experimental results and parameter analysis of the simulated and real datasets. Finally, Section V concludes the study.

II. NOTATIONS AND PROBLEM FORMULATION

A. NOTATIONS

Bold lowercase letters (e.g., x) denote vectors, uppercase letters (e.g., X) denote matrices, and calligraphic letters (e.g.,$\mathcal{X}$) denote tensors. A tensor is a multi-dimensional data structure, and an n-dimensional tensor ($n \geq 3$) is denoted using a calligraphic symbol such as $\mathcal{X} \in \mathbb{R}^{I_1 \times I_2 \times I_3 \times \ldots \times I_n}$. The value of an element in position $(i_1, i_2, \ldots, i_n)$ is represented as $\mathcal{X}(i_1, i_2, \ldots, i_n)$ or $\mathcal{X}_{i_1,i_2,\ldots,i_n}$. This study adopts a type of tensor metrication, also known as unfolding, which is defined as follows: In [26], the concept of normal mode-k unfolding of a tensor is introduced and denoted as Moreover, the Frobenius norm of tensor x can be computed as $||\mathcal{X}||_F$: $(\sum_{i,j,s} |\mathcal{X}(i,j,s)|^2)^{1/2}$.

B. HSI DENOISING VIA TENSOR DECOMPOSITION

The problem of image noise reduction is difficult because it is frequently poorly posed. HSI signal restoration can be expressed as a mathematical optimisation problem with regularisation. The noisy HSI can be depicted as an addition of a noise component and a pure HSI, where is the width and length of the image and is the count of the spectral channels. Based on its intensity distribution characteristics,

this noise can be portrayed as a mixture of stochastic and sparsity-induced noise. Consequently, the corrupted hyperspectral image can be represented as a displacement of the denoised image, and the denoising challenge can be considered a barrier to inferring the denoised hyperspectral image from noisy observations.

$$\mathcal{Y} = \mathcal{X} + \mathcal{N} + \mathcal{S} \tag{1}$$

The task of denoising hyperspectral images (HSIs) based on the degradation model (1) is difficult and usually involves recovering a clean signal from a noisy observation. Owing to the complex nature of this issue, it is often considered poorly posed. Therefore, to solve the difficult and ambiguous problem of eliminating noise from hyperspectral images, a regularisation framework can be used by incorporating prior knowledge of HSI. This framework can be described as follows:

$$\arg\min J(\mathcal{X}, \mathcal{S}, \mathcal{N}) + \beta R(\mathcal{X}) \tag{2}$$

where $J(\mathcal{X}, \mathcal{S}, \mathcal{N})$ denotes the distribution characteristics of various noises; $R(\mathcal{X})$ represents the prior information of the unknown clean HSI; β denotes a non-negative regularisation parameter used to balance the two regularisation terms. In the regularisation framework, both the prior information and the noise distribution are crucial, in determining the accuracy of the recovery result.

Using a low-rank prior for HSI, the regularisation framework can be straight-forwardly stated as follows:

$$\min_{\mathcal{X},\mathcal{N},\mathcal{S}} rank(\mathcal{X}) + \lambda_1 ||\mathcal{N}||_F^2 + \lambda_2 ||\mathcal{S}||_1 \tag{3}$$

where $rank(\mathcal{X})$ represent the tensor rank, λ_1 and λ_2 are regularisation parameters.

Based on Model (3), the critical issue in restoring the hyperspectral image from the noisy image more precisely and effectively is to design suitable regularisation constraints to recover the hyperspectral image. Numerous tensor-based methods use tensor low-rank decomposition to denoise the hyperspectral image since the hyperspectral image is a three-dimensional tensor instead of a two-dimensional image. This involves the use of methods based on low matrix and tube ranks to denoise HSIs.

A degraded image may contain both original image information and noise information, and the original image information can be considered as an array of data with reduced dimensionality. The rank can be used to indicate the degree of information included in an image. As described by the matrices, an image can be denoted as a matrix, and if the figure of linearly independent vectors that correspond to the matrix is small, the matrix's rank is also small, suggesting that the image is low-rank. Based on mathematical knowledge, if the rows or columns of a matrix can be linearly represented by other rows or columns, then it can be deduced that the matrix (image) contains a significant amount of redundant information. Thus, redundant information in these low-rank matrices can be used for image denoising and the reconstruction of clean images.

In denoising HSI by defining tensor tube rank, tensor singular value decomposition (t-SVD) has proved effective. However, the t-SVD method has limits in its ability to handle varied correlations in various modes of HSI, which can cause suboptimal denoising results. Specifically, t-SVD uses SVD to capture spatial correlations and circular convolution for spectral correlations, which may not be adequately flexible to capture all forms of correlations. This unyielding HSI representation often results in suboptimal denoising performance. The flexible handling of each mode is predicted to compensate for this inadequacy.

These methods use the inter-band correlation present in the HSI to decrease spatial-spectral redundancy. However, the direct application of tensor-based representations to complete HSI data limits the investigation of non-local self-correlation priors [29]. Recently, it was shown that non-local methods achieve the best results in denoising HSIs [28], [29], [30], [32]. Similar to the regularised model for whole HSI denoising, the following optimisation formulation can be employed to maximise a non-local HSI denoising model:

$$\arg\min J(\mathcal{X}, \mathcal{S}, \mathcal{N}) + \beta R(\mathcal{X}_i) \tag{4}$$

The crucial issue, similar to model (3), is to explore the preceding knowledge of $\mathcal{X}_i$ and design relevant regularisations for the optimised model (4). The global correlation can be explored through patch clustering based on similarity both in spectral and non-local patterns. To investigate these correlations, numerous denoising methods consider the spatial-spectral NSS before HSIs, i.e. considering similar three-dimensional cubes instead of two-dimensional image patches as the fundamental entity for denoising, including BM4D [34], MSPCA-BM3D [35], methods based on non-local TDL [28], and methods based on ITS regularisation [29].

III. PROPOSED NON-LOCAL 3DLOGTNN DECOMPOSITION FOR HSI DENOISING

Despite the satisfactory results attained by the non-local tensor-based HSI denoising methods mentioned above, there is still potential for further advancement. Zheng et al. suggested a 3DLogTNN algorithm [26] that can process each channel in 3D hyperspectral data while considering the spectral information in the 3D data, resulting in better extraction of both local and global information. This method is distinctive for its significantly accurate and flexible low-rank scatter representation of HSI. This approach can retain the structure more effectively, unlike matrix low-rank-based methods that involve unfolding operations and may not maintain the inherent structure of information. In addition, compared with tubal low-rank-based methods, it can fully and directly leverage both spatial and spectral correlations, improving denoising performance.

A. 3DLOGTNN DECOMPOSITION

The uniqueness of the 3DLogTNN model lies in its extension of t-SVD to modal kt-SVD, introducing a new tensor rank named tensor-fibered rank and improving a more adaptable and accurate representation of the HSI. It also uses a new regularisation term called the three-dimensional tensor nuclear norm that can make the most of the structural characteristics of high-dimensional spectral images and offer useful constraints for decomposing both low-rank and sparse components.

As mentioned earlier, the t-SVD method has drawbacks when it comes to handling different correlations in various dimensions of HSIs, resulting in an incomplete representation of the spectral modes. To overcome this drawback, the 3DLogTNN method proposes a mode-k-tensor singular value decomposition (mode-kt-SVD) approach.

Theorem 1 (Mode-k t-SVD): A three-dimensional tensor $\mathcal{X} \in \mathbb{R}^{n_1 \times n_2 \times n_3}$ can be decomposed into a multilinear factorization form as follows:

$$\mathcal{X} = \mathcal{U}_{k*k}\mathcal{S}_{k*k}\mathcal{V}_k^{T_k}$$

where $\mathcal{U}_K$ and $\mathcal{V}_K$ denote the mode-k orthogonal tensors and $\mathcal{S}_K \in \mathbb{R}^{n_1 \times n_2 \times n_3}$ denotes the mode-k diagonal tensor.

Considering the different observation degradations due to diverse noise reduction techniques. In this study, the HSI denoising method introduced using the prior assumption of a low fibre rank can be mathematically expressed as follows:

$$\begin{aligned} &\min_{\mathcal{X},\mathcal{N},\mathcal{S}} rank_f(\mathcal{X}) + \lambda_1 ||\mathcal{N}||_F^2 + \lambda_2 ||\mathcal{S}||_1 \\ &\mathcal{Y} = \mathcal{X} + \mathcal{N} + \mathcal{S} \end{aligned} \tag{5}$$

where $\mathcal{X} \in \mathbb{R}^{n_1 \times n_2 \times n_3}$ denotes the fundamental HIS, $\mathcal{Y}$ denotes the noisy hyperspectral image, $\mathcal{N}$represents the Gaussian noise, $\mathcal{S}$ denotes the sparse noise,and $\lambda 1$ and $\lambda 2$ denote the regularisation parameters.

We define the following definition of tensor-fibered rank, combining the fibre rank of all modes k. However, the tensor tubal rank represents the fibre rank of the third axis of a tensor.

Definition 1 (Tensor Fibered Rank): The fibered rank of a three-dimensional tensor $\mathcal{X} \in \mathbb{R}^{n_1 \times n_2 \times n_3}$, is given by a vector, denoted as $rank_f(\mathcal{X})$, where the kth element represents the mode-k tensor-fibered rank.

Because directly minimising the proposed fibered rank is NP-hard, the 3DLogTNN is introduced as a non-convex variant of the proposed fibered rank relaxation to provide a suitable computational approach.

Definition 2 (Mode-k LogTNN): The tensor nuclear norm based on the mode-k logarithm of a tensor $\mathcal{X} \in \mathbb{R}^{n_1 \times n_2 \times n_3}$ is defined as:

$$LogTNN_k(\mathcal{X}, \varepsilon) := \sum_{i=1}^{n_k} LogMNN((\overline{X}_k)_k^{(i)}, \varepsilon)$$

where $(\overline{X}_k)_k^{(i)}$ denotes the i th mode-k slice of $\overline{\mathcal{X}}_k$ with $\overline{\mathcal{X}}_k = \text{fft}(\mathcal{X}, [], k)$ and $LogMNN(X, \varepsilon) := \sum_{i=1}^{m} Log(\sigma_i(X) + \varepsilon)$.

Definition 3 (3DLogTNN): The 3DLogTNN of a tensor $\mathcal{X} \in \mathbb{R}^{n_1 \times n_2 \times n_3}$ is defined as:

$$3DLogTNN(\mathcal{X}, \varepsilon) := \sum_{k=1}^{3} \omega_k LogTNN_k(\mathcal{X}, \varepsilon)$$

where $\omega_k \geqslant 0 (k = 1, 2, 3)$ and $\sum_{k=1}^{3} \omega_k = 1$.

Under the definition of 3DLogTNN, the proposed HSI denoising model based on 3DLogTNN is typically formulated as:

$$\begin{aligned} &\min_{\mathcal{X},\mathcal{N},\mathcal{S}} \sum_{k=1}^{3} \omega_k \mathcal{R}_k(\mathcal{X}) + \lambda_1 ||\mathcal{N}||_F^2 + \lambda_2 ||\mathcal{S}||_1 \\ &s.t. \mathcal{Y} = \mathcal{X} + \mathcal{N} + \mathcal{S} \end{aligned} \tag{6}$$

where the function $\mathcal{R}_k(\mathcal{X})$ is set to be $LogTNN_k(\mathcal{X}, \varepsilon)$ in the 3DLogTNN-based HSI denoising model, respectively.

B. NON-LOCAL 3DLOGTNN DECOMPOSITION MODEL

The definition and characteristics of 3DLogTNN factorisation show numerous advantages compared with alternative tensor factorisation techniques. First, the 3DLogTNN algorithm is a tensor decomposition-based method that can handle three-dimensional hyperspectral data more flexibly while maintaining a certain degree of low rankness. However, when processing hyperspectral data, other tensor decomposition methods may excessively compress or stretch specific directions of the data, which results in the underutilisation of data features. Second, the 3DLogTNN algorithm can process each channel in three-dimensional hyperspectral data while considering the spectral information in the data, improving global feature extraction. Other tensor decomposition methods can only handle one channel in hyperspectral data and cannot fully consider spectral information in three-dimensional data. Third, when processing hyperspectral data, the 3DLogTNN algorithm is more robust and generalisable because of the use of low-rank regularisation that reduces noise. Compared with other tensor decomposition methods, the 3DLogTNN algorithm is more sensitive to noise and can better handle hyperspectral data with strong noise.

Based on the benefits of 3DLogTNN decomposition, we propose a high-dimensional method for eliminating mixed noise named NL3DLogTNN, which considers both global spectral low rankness and spectral association, and captures non-local self-resemblance. To capture the overall spectral concordance, we specifically use the 3DLogTNN model to match the groups of similar image blocks in high-dimensional space using a non-local framework. Therefore, the proposed method can be characterised as:

$$\begin{aligned} &\min_{\mathcal{X}_i,\mathcal{N}_i,\mathcal{S}_i} \sum_{k=1}^{3} \omega_k \mathcal{R}_k(\mathcal{X}_i) + \lambda_1 ||\mathcal{N}_i||_F^2 + \lambda_2 ||\mathcal{S}_i||_1 \\ &s.t. \mathcal{Y}_i = \mathcal{X}_i + \mathcal{N}_i + \mathcal{S}_i \end{aligned} \tag{7}$$

The proposed method composes three components: exploiting low-fibered-rank tensor decomposition to represent

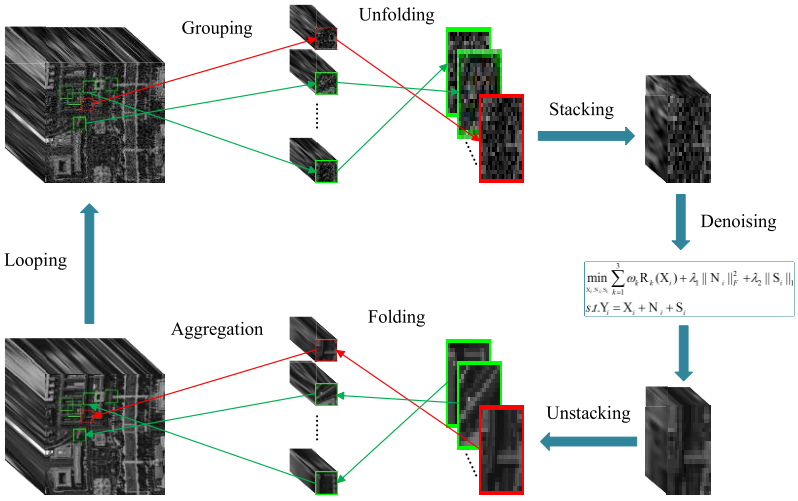

FIGURE 2. Framework of the proposed HSI denoising method.

topographical non-local self-resemblance and high correlation among feature images, incorporating F-norm to account for Gaussian noise, and employing the norm term to handle sparse noise.

The NL3DLogTNN method consists of four main steps:

1) For each local block, use KNN to search for its similar blocks;

2) Perform an unfolding operation to combine identical blocks from the same cluster into a three-dimensional tensor Xi;

3) Perform low-rank tensor decomposition in three directions for denoising, obtaining Yi;

4) Perform a fold inverse operation to restore it to the original local tensor block.

This method involves unfolding and stack operations. Let $\mathcal{X} \in \mathbb{R}^{s\times s\times b}$ denote the 3-D patches of I, where s denotes the spatial size of the 3-D patch and b denotes the spectral dimension. The fold operation unfolds each 3-D patch into a 2-D matrix of size $s^2 \times b$, whereas the stack operation stacks the 2-D matrices obtained by unfolding the 3-D patches in the same similarity cluster along the third dimension to reconstruct a $s^2 \times b \times k$ three-dimensional tensor. Please refer to the flowchart for a better understanding of these operations.

The Integration of the 3DLogTNN algorithm and non-local self-resemblance led to a substantial improvement in the denoising performance of the proposed methodology. Non-local self-resemblance allows the extraction of texture and structural information from the image, further reducing the impact of noise. Simultaneously, in the process of low-rank tensor decomposition of the 3DLogTNN, using NSS can also improve the effectiveness of low-rank factorisation and capture both local and global features more efficiently. Compared to combining other tensor decomposition methods with non-local self-resemblance, combining the 3DLogTNN algorithm with NSS has higher flexibility, better denoising performance, and robustness, and can handle hyperspectral image data better.

C. OPTIMIZATION METHOD AND CONVERGENCE ANALYSIS

Model (7) is solved using the ADMM, which involves introducing three additional variables $\mathcal{I}_k (k = 1, 2, 3)$ to transform the model into an equivalent form. Thus, the problem can be reformulated as:

$$\begin{aligned}&\min_{\mathcal{X}_i,\mathcal{N}_i,\mathcal{S}_i} \sum_{k=1}^{3} \omega_k \mathcal{R}_k(\mathcal{X}_i) + \lambda_1 ||\mathcal{N}_i||_F^2 + \lambda_2 ||\mathcal{S}_i||_1 \\ &s.t. \begin{cases} \mathcal{Y}_i - (\mathcal{X}_i + \mathcal{N}_i + \mathcal{S}_i) = 0 \\ \mathcal{X}_i - \mathcal{I}_k = 0, k = 1, 2, 3 \end{cases}\end{aligned} \tag{8}$$

The augmented Lagrangian function of (8) is

$$\begin{aligned}&L_{\alpha_k,\beta}(\mathcal{I}_k, \mathcal{X}_i, \mathcal{N}_i, \mathcal{S}_i, \mathcal{M}_k, \mathcal{V}) \\ &= \sum_{k=1}^{3} \left\{ \omega_k \mathcal{R}_k(\mathcal{I}_K) + \langle \mathcal{X}_i - \mathcal{I}_K, \mathcal{M}_k \rangle + \frac{\alpha_k}{2} ||\mathcal{X}_i - \mathcal{I}_K||_F^2 \right\} \\ &\quad + \lambda_1 ||\mathcal{N}_i||_F^2 + \lambda_2 ||\mathcal{S}_i||_1 + \langle \mathcal{Y}_i - (\mathcal{X}_i + \mathcal{N}_i + \mathcal{S}_i), \mathcal{V} \rangle \\ &\quad + \frac{\beta}{2} ||\mathcal{Y}_i - (\mathcal{X}_i + \mathcal{N}_i + \mathcal{S}_i)||_F^2\end{aligned} \tag{9}$$

where $\mathcal{M}_k (k = 1, 2, 3)$ and $\mathcal{V}$ represent the Lagrange multipliers; $\alpha_k (k = 1, 2, 3)$ and β represent the penalty parameters. Within the framework of ADMM, $\mathcal{I}_k, \mathcal{X}_i, \mathcal{N}_i, \mathcal{S}_i, \mathcal{M}_k$, and $\mathcal{V}$ are alternately updated as:

$$\begin{cases} \mathcal{I}_k^{t+1} = \arg\min_{E_k} L_{\alpha_k,\beta}(\mathcal{I}_k, \mathcal{X}_i^t, \mathcal{N}_i^t, \mathcal{S}_i^t, \mathcal{M}_k^t, \mathcal{V}^t) \\ \mathcal{X}_i^{t+1} = \arg\min_{\mathcal{X}_i} L_{\alpha_k,\beta}(\mathcal{I}_k^{t+1}, \mathcal{X}_i, \mathcal{N}_i^t, \mathcal{S}_i^t, \mathcal{M}_k^t, \mathcal{V}^t) \\ \mathcal{N}_i^{t+1} = \arg\min_{\mathcal{N}_i} L_{\alpha_k,\beta}(\mathcal{I}_k^{t+1}, \mathcal{X}_i^{t+1}, \mathcal{N}_i, \mathcal{S}_i^t, \mathcal{M}_k^t, \mathcal{V}^t) \\ \mathcal{S}_i^{t+1} = \arg\min_{\mathcal{S}_i} L_{\alpha_k,\beta}(\mathcal{I}_k^{t+1}, \mathcal{X}_i^{t+1}, \mathcal{N}_i^{t+1}, \mathcal{S}_i, \mathcal{M}_k^t, \mathcal{V}^t) \\ \mathcal{M}_k^{t+1} = \mathcal{M}_k^t + \alpha_k(\mathcal{X}_i^{t+1} - \mathcal{I}_k^{t+1}) \\ \mathcal{V}^{t+1} = \mathcal{V}^t + \beta(\mathcal{Y}_i - \mathcal{X}_i^{t+1} - \mathcal{N}_i^{t+1} - \mathcal{S}_i^{t+1}) \end{cases} \tag{10}$$

We introduce two theorems to further solve (10):

Theorem 2 (Mode-k TNN-Based t-SVT): Assuming that $\mathcal{I} \in \mathbb{R}^{n_1 \times n_2 \times n_3}$ is a three-way tensor, a minimizer to

$$\arg\min_{\mathcal{I}} \tau ||\mathcal{I}||_{TNN_k} + \frac{1}{2}||\mathcal{I} - \mathcal{Y}||_F^2$$

is represented using mode-k tensor nuclear norm-based tensor singular value thresholding (TNN-based t-SVT).

$$\mathcal{I} = \mathcal{D}_{tnn}^{\tau}(\mathcal{Y}, k) := \mathcal{U}_{*k}\mathcal{S}_{tnn}^{\tau_{*k}}\mathcal{V}^{T_k}$$

Theorem 3 (Mode-k LogTNN-Based t-SVT): Suppose that is a three-way tensor. Then, a solution that minimizes the following expression is sought:

$$\arg\min_{\mathcal{Z}} \tau LogTNN_k(\mathcal{Z}, \varepsilon) + \frac{1}{2}||\mathcal{Z} - \mathcal{Y}||_F^2$$

is obtained by employing the mode-k LogTNN-based tensor singular value thresholding (t-SVT) method.

$$\mathcal{I} = \mathcal{D}_{1t}^{\tau,\varepsilon}(\mathcal{Y}, k) := \mathcal{U}_{*k}\mathcal{S}1t_{*k}^{\tau,\varepsilon}\mathcal{V}^{T_k}$$

We can use Theorems 2 and 3 to solve the $\mathcal{I}_k (k = 1, 2, 3)$ subproblems in the proposed HSI method based on NL3DLogTNN, which can be expressed as

$$\mathcal{I}_k^{t+1} = \mathcal{D}_{1t}^{\frac{\omega_k}{\alpha_k},\varepsilon}(\mathcal{X}_i^t + \frac{\mathcal{M}_k^t}{\alpha_k}, k) \tag{11}$$

Theorem 3 can easily be proven using [29] (Th. 2).

Drawing on the above solving strategy, the subproblem of $\mathcal{X}, \mathcal{N}, \mathcal{S}$ is

$$\begin{cases} \mathcal{S}_i^{t+1} = shrink\left(\mathcal{Y}_i - \mathcal{X}_i^{t+1} - \mathcal{N}_i^{t+1} + \frac{\mathcal{V}^t}{\beta}, \frac{\lambda_2}{\beta}\right) \\ \mathcal{X}_i^{t+1} = \frac{\sum_{k=1}^{3} \alpha_k \left(\mathcal{I}_k^{t+1} - \frac{\mathcal{M}_k^t}{\alpha_k}\right) + \beta\left(\mathcal{Y}_i - \mathcal{N}_i^t - \mathcal{S}_i^t + \frac{\mathcal{V}^t}{\beta}\right)}{\sum_{k=1}^{3} \alpha_k + \beta} \\ \mathcal{N}_i^{t+1} = \frac{\beta\left(\mathcal{Y}_i - \mathcal{X}_i^{t+1} - \mathcal{S}_i^t + \frac{\mathcal{V}^t}{\beta}\right)}{2\lambda_1 + \beta} \end{cases} \tag{12}$$

where $shrink(., \zeta)$ is the tensor soft thresholding operator with threshold ζ, that is,

$$[shrink(\mathcal{X}, \zeta)]_{ijs} = \text{sgn}(x_{ijs}) \max(|x_{ijs}| - \zeta, 0). \tag{13}$$

Algorithm 1 summarises the entire HSI denoising process. Based on the optimisation algorithm framework in reference [34], this algorithm can optimise the objective function's point during convergence. The proposed approach is anticipated to achieve a crucial stage of the objective function during convergence.

D. COMPUTATIONAL COMPLEXITY

The time complexity to compute all local blocks for a noisy tensor $\mathcal{Y}$ with the size $M \times N \times C$ is $O(MN)$. For each tensor block formed by stacking each similar cluster, denoted as $\mathcal{Y}_i$, with size $n_1 \times n_2 \times n_3$ (where n_1 represents the block size and n_2 represents the spectral size, and n_3 represents the number of blocks included in the similar cluster), the time complexity of tensor decomposition is:

$$O(n_1 n_2 n_3(\log(n_1 n_2 n_3) + \sum_{i=1}^{3} \min(n_i, n_{i+1}))).$$

Thus, in this study, the total time complexity of the proposed model is $O(MNO(n_1 n_2 n_3(\log(n_1 n_2 n_3) + \sum_{i=1}^{3} \min(n_i, n_{i+1}))))$.

Despite the relatively high time complexity of the proposed model, it exhibits good denoising performance for mixed noise. Furthermore, since the reconstruction of each non-local similar block is an independent task that does not affect each other, parallel computing can be utilized to reduce the computational time of the model. Additionally, the use of grouping preprocessing techniques can also reduce the time consumption in the similar block matching stage.

Algorithm 1 NL3DLogTNN Method for HSI Denoising

Input: The noisy HSI Y, parameters $\alpha = (\alpha 1, \alpha 2, \alpha 3)$, P, K, $\delta = 0.1$.
Initialisation: Let $\mathcal{X}^{(0)} = \mathcal{Y}$, $\mathcal{Y}^{(0)} = \mathcal{Y}$.
1: **for** $j = 1: J$ **do**
2: Calculate $\mathcal{Y}^{(j)} = \mathcal{Y}^{(j-1)} + \delta(\mathcal{Y} - \mathcal{X}^{(j-1)})$.
3: **for** each exemplar patch Y_i **do**
4: The grouping of non-local similar patches to form a tensor Y_i.
5: Initialise $\mathcal{X}_i^{(0)} = 0$, $\mathcal{N}_i^{(0)} = 0$, $\mathcal{S}_i^{(0)} = 0$, $\mathcal{I}_k{}^{(0)} = 0$, $\mathcal{M}_k{}^{(0)} = 0$, $\mathcal{V}^{(0)} = 0$.
6: **for** $t = 1: T$ **do**
7: Update $\mathcal{I}_k{}^{(t+1)} via(11), k = 1, 2, 3$.
8: Update $\mathcal{X}_i^{(t+1)}, \mathcal{N}_i^{(t+1)}, \mathcal{S}_i^{(t+1)} via(12)$.
9: Update $\mathcal{M}_k{}^{(t+1)}, \mathcal{V}^{(t+1)} via(10)$.
10: **end for**
11: **end for**
12: Aggregate all $\mathcal{X}_i$ to achieve the denoised HSI $\mathcal{X}^{(j)}$.
13: **end for**
Output: Denoise HIS result $\mathcal{X}^{(j)}$.

IV. EXPERIMENTAL RESULTS AND DISCUSSION

We performed experimental tests on both simulated and real data to assess the result of the proposed NL3DLogTNN model for denoising HSI in the presence of degradation. We assessed the validity of our proposed NL3DLogTNN model on both simulated and real HSI datasets and compared it with six existing denoising methods that are extensively recognised as state-of-the-art and representative methods: NLTR [36], LRTDTV [20], LRTDGS [18], 3DTNN [26], 3DLogTNN [26] and FGSLR$_{1/2}$ [45]. To ensure optimal denoising performance, we carefully read the papers on each model and selected the recommended parameter combinations in line with the recommendations of the authors. The patch size P = 25 and the number of similar patches K = 200 were employed for all experiments. Section IV-C

provides a comprehensive analysis of the parameter selection for the NL3DLogTNN. δ was set to 0.1, and the other parameters were robust and consistent with those in the 3DLogTNN.

Since the noise in HSIs is often an amalgamation of various noise types commonly encountered in real-world scenarios, we investigated the following five scenarios:

Case 1 (Gaussian noise): Apply zero-mean Gaussian noise with a standard deviation randomly selected from the range [0.1, 0.2] to all spectral bands of the hyperspectral image.

Case 2 (Gaussian noise + salt-and-pepper noise): Similar to Case 1, Gaussian noise with the same settings was added to all bands. Additionally, salt-and-pepper noise with a noise ratio randomly selected from the range [0.2, 0.3] was added to all the bands.

Case 3 Case 3 (Gaussian Noise + Salt-and-Pepper Noise + Stripe): The process for adding Gaussian noise and salt-and-pepper noise is identical to that in Case 2. In addition, we added stripes at random to 40% of the images. The number of stripes inserted in every selected region was randomly selected from the set [15, 6, 7,...]. In particular, if a column was selected for stripe addition, all entries in the column were assigned a value randomly selected from the range [0.6, 0.8].

Case 4 (Gaussian Noise + Salt-and-Pepper Noise +Deadline): The procedure for adding Gaussian noise and salt-and-pepper noise is similar to that in Case 2. Furthermore, 20% of the total bands were randomly selected, and stripes of a randomly selected width were added from the set [1], [2], [3]. The number of stripes in each selected band was randomly chosen from the set [10, 6, 7,...]. If a column is selected for the introduction of stripes, all the elements in that column are set to zero.

Case 5 (Gaussian Noise + Salt-and-Pepper Noise + Stripe + Deadline): The addition of Gaussian noise and salt-and-pepper noise is similar to that in Case 2. Additionally, in cases 3 and 4 the same procedure for the introduction of stripes and dead pixels is involved.

A. MIXED NOISE REMOVAL ON SIMULATED DATA

In this section, we evaluate the validity of contrastive denoising models using three extensively employed hyperspectral imaging datasets: Pavia City Center, Washington DC Mall and CAVE. We conducted an evaluation of various models' denoising performance on subsets of three datasets. Specifically, we selected subsets from the City Center and Washington DC Mall datasets, with dimensions of $200\times200\times50$ each. Additionally, we chose a subset from the CAVE dataset, specifically the balloons image, to assess the models' performance on larger-scale data. The size of this subset was set to $350\times350\times50$ to provide a comprehensive evaluation of the models' capabilities in handling larger image sizes under different noise conditions. We employ three objective metrics, namely peak signal-to-noise ratio (PSNR), structural similarity (SSIM), and spectral angle mapper (SAM), to comprehensively evaluate the denoising results. PSNR and SSIM have commonly employed metrics for image restoration, whereas SAM is based on a spectral evaluation. Higher PSNR and SSIM values show a better denoising performance, whereas smaller SAM values show better results. Furthermore, we present denoised images for visual comparison.

1) Quantitative Comparison: Table 1 presents the quantitative results for five various noise scenarios in the two datasets. We obtained the MPSNR, MSSIM, and MSAM indicators by calculating the central tendencies of the PSNR, SSIM, and SAM for all bands.

Table 1 shows we gauged the performance of our proposed NL3DLogTNN approach against six widely employed and advanced denoising methods under different noise conditions in the three datasets. The experimental results showed that the NL3DLogTNN model performed excellently in all the noise scenarios. In the Pavia City Center dataset, the NL3DLogTNN model performed particularly well in Case 3, Case 4, and Case 5 noise scenarios, with MPSNR and MSSIM scores reaching the optimal level. In the Washington DC Mall dataset, the NL3DLogTNN model accomplished the highest MPSNR score in the Case 1-5, noise scenarios, while some MSSIM and MSAM scores were slightly below the optimal level but were still comparable. In the Cave-Balloons dataset, due to the pronounced low-rank prior and non-local prior of this dataset, the NL3DLogTNN model exhibited excellent denoising performance in all five noise scenarios. The MPSNR and MSSIM scores reached the optimal level, with only slightly lower MSAM scores in Case 4 and Case 5 scenarios compared to the FGSLR1/2 model of 2022. Furthermore, even though the NL3DLogTNN model's denoising performance did not reach the optimal level in some specific noise scenarios, it demonstrated good denoising performance in all types of noise scenarios and therefore outperformed other models in comprehensive denoising performance.

Figure 3 shows the PSNR values of each band after denoising under various noise conditions. The proposed model outperformed the compared models in terms of PSNR measurements for each band under various noise conditions. This indicates that the NL3DLogTNN model exhibits superior denoising performance across various scenarios, leading to an overall improvement in the denoising performance.

2) Qualitative Comparison: Figures 4-6 visually demonstrate the denoising results of each model in the Case 3 scenario using the Pavia City Center dataset, Washington DC Mall dataset, and CAVE-Balloons dataset. By zooming in on local denoising effects, these figures provide a more intuitive comparison of the recovery outcomes in terms of visual perception.

In the Pavia City Center dataset, all the models compared could efficiently eliminate Gaussian noise and salt-and-pepper noise. However, NLTR, 3DTNN, and 3DLogTNN failed to completely eliminate the stripe noise. NLTR is a model based on a non-local prior that partially eliminates stripe noise; however, some residues remain globally. 3DTNN and 3DLogTNN are built upon low-rank tensor decomposition, which has a limited effect on stripe denoising but indicates clearer local details. On the other hand,

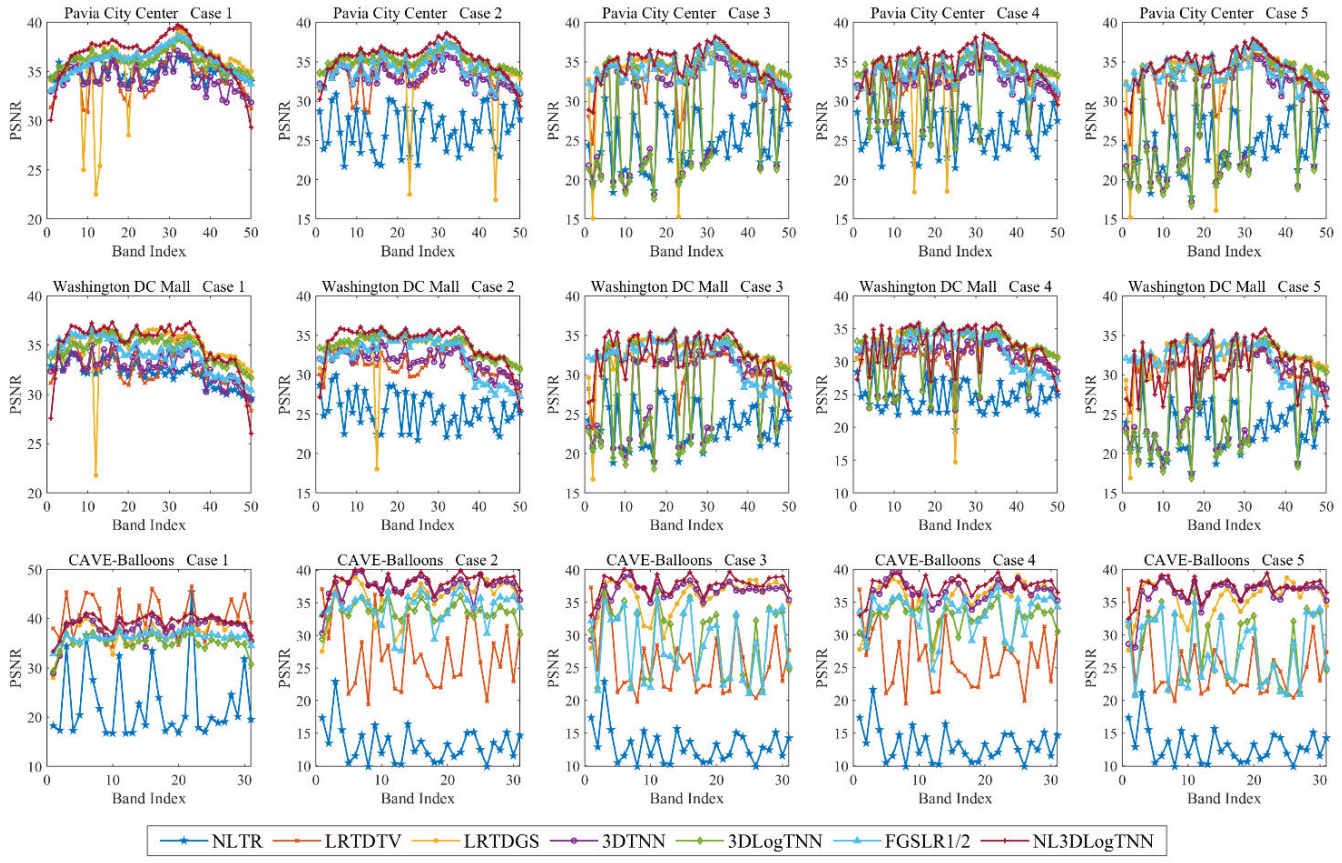

FIGURE 3. Quantitative comparison of seven denoising models over all spectral bands under various noise levels.

the proposed NL3DLogTNN model performs well in global noise removal and also shows clearer local details, which is more similar to a clean image and has better denoising performance.

Regarding the Washington DC Mall dataset, except for NLTR, 3DTNN, and 3DLogTNN, most of the compared models can eliminate blended noise effectively, whereas the three models were ineffective in removing stripe noise. Although having slightly lower scores on some metrics compared to the best model, the overall denoising performance of the recommended NL3DLogTNN model outperformed that of all other models. Additionally, the NL3DLogTNN model demonstrated superior visual results in terms of preserving the global structure and local details, highlighting its robust stability and excellent performance.

Regarding the CAVE dataset, except for NLTR, 3DTNN, and 3DLogTNN, most of the compared models efficiently eliminate mixed noise, while the three models were inefficient in removing striped noise. Although having achieved slightly lower scores on certain metrics compared to the top-performing model, the overall denoising performance of the recommended NL3DLogTNN model surpassed that of all other models. Furthermore, the NL3DLogTNN model exhibited superior visual outcomes in terms of preserving the overall structure and intricate details, showcasing its robust stability and outstanding performance

B. MIXED NOISE REMOVAL ON REAL DATA

The experiments described above-involved simulations to test the efficacy of the NL3DLogTNN method. However, in practical situations, the noise distortion is substantially more complicated. Thus, we chose two well-known datasets with real noise for testing to demonstrate the NL3DLogTNN's ability to handle real-world HSI noise: the WHU HongHu dataset with a size of $940\times475\times270$, and the HYDICE Urban dataset with a size of $307\times307\times210$.

oth of these datasets consist of Gaussian noise, salt-and-pepper noise, stripe noise, and deadline noise. We selected a subset of 50 consecutive spectral bands with severe noise from these two datasets for experiments, with sizes of $200\times200\times50$ and $200\times200\times50$, because some bands only have a relatively small amount of real noise.

Figure 7 demonstrates that all seven compared models effectively removed Gaussian and salt-and-pepper noise on the WHU HongHu dataset when compared to the initial noisy image. However, the other six models were unable to completely eliminate stripe and deadline noise. In contrast, the proposed NL3DLogTNN method successfully eliminated

TABLE 1. Performance comparison of 7 denoising models under different noise conditions.

Dataset	Case	Index	Noisy	NLTR	LRTDTV	LRTDGS	3DTNN	3DLogTNN	FGSLR$_{1/2}$	Ours
Pavia City Center	Case 1	MPSNR	24.030	34.994	34.838	35.648	34.221	36.152	36.095	**36.622**
		MSSIM	0.563	0.958	0.949	0.946	0.962	**0.972**	0.970	0.971
		MSAM	24.553	2.873	3.163	5.292	2.466	**2.203**	2.739	2.833
	Case 2	MPSNR	13.617	26.442	33.469	34.217	33.128	35.183	34.018	**35.484**
		MSSIM	0.208	0.824	0.933	0.930	0.951	**0.965**	0.956	0.963
		MSAM	38.865	7.199	3.763	7.321	2.707	**2.409**	3.007	3.001
	Case 3	MPSNR	13.374	24.641	33.312	33.943	28.234	29.223	33.882	**34.660**
		MSSIM	0.201	0.755	0.928	0.926	0.863	0.873	0.954	**0.961**
		MSAM	38.858	9.820	4.316	8.658	11.585	12.393	**3.180**	3.464
	Case 4	MPSNR	13.591	26.148	33.154	33.862	31.503	33.066	33.766	**34.866**
		MSSIM	0.205	0.808	0.931	0.929	0.925	0.937	0.955	**0.962**
		MSAM	39.325	8.090	4.004	7.245	5.743	6.130	**3.280**	3.600
	Case 5	MPSNR	13.363	24.336	33.021	33.710	27.272	28.098	33.763	**34.272**
		MSSIM	0.199	0.731	0.925	0.925	0.835	0.845	0.954	**0.959**
		MSAM	39.320	10.829	4.464	8.521	13.661	14.737	**3.313**	3.747
Washington DC Mall	Case 1	MPSNR	24.030	32.121	32.719	34.848	32.838	34.697	34.045	**35.079**
		MSSIM	0.621	0.940	0.941	0.957	0.961	**0.970**	0.964	0.966
		MSAM	20.475	3.411	2.863	3.833	3.167	**2.719**	3.056	3.282
	Case 2	MPSNR	13.696	25.446	31.331	33.160	31.813	33.745	32.267	**34.001**
		MSSIM	0.270	0.808	0.923	0.938	0.951	**0.962**	0.947	0.957
		MSAM	35.142	7.582	3.358	4.942	3.489	**2.976**	3.636	3.591
	Case 3	MPSNR	13.483	23.453	31.034	32.912	27.653	28.450	32.027	**32.700**
		MSSIM	0.263	0.724	0.915	0.936	0.877	0.884	0.946	**0.949**
		MSAM	35.218	10.206	4.006	5.178	9.586	10.345	**3.820**	4.316
	Case 4	MPSNR	13.624	24.561	30.936	32.633	30.105	31.649	31.958	**32.682**
		MSSIM	0.266	0.777	0.919	0.933	0.924	0.936	0.946	**0.950**
		MSAM	35.705	9.017	**3.687**	5.886	6.114	5.997	3.862	4.597
	Case 5	MPSNR	13.432	22.848	30.727	32.559	26.644	27.346	**31.865**	31.366
		MSSIM	0.259	0.694	0.913	0.932	0.850	0.858	**0.945**	0.936
		MSAM	35.761	11.573	3.821	5.381	11.589	12.427	**3.926**	5.410
CAVE-Balloons	Case 1	MPSNR	24.030	34.994	34.838	35.648	34.221	36.152	36.095	**36.622**
		MSSIM	0.563	0.958	0.949	0.946	0.962	**0.972**	0.970	0.971
		MSAM	24.553	2.873	3.163	5.292	2.466	**2.203**	2.739	2.833
	Case 2	MPSNR	13.617	26.442	33.469	34.217	33.128	35.183	34.018	**35.484**
		MSSIM	0.208	0.824	0.933	0.930	0.951	**0.965**	0.956	0.963
		MSAM	38.865	7.199	3.763	7.321	2.707	**2.409**	3.007	3.001
	Case 3	MPSNR	13.374	24.641	33.312	33.943	28.234	29.223	33.882	**34.660**
		MSSIM	0.201	0.755	0.928	0.926	0.863	0.873	0.954	**0.961**
		MSAM	38.858	9.820	4.316	8.658	11.585	12.393	**3.180**	3.464
	Case 4	MPSNR	13.591	26.148	33.154	33.862	31.503	33.066	33.766	**34.866**
		MSSIM	0.205	0.808	0.931	0.929	0.925	0.937	0.955	**0.962**
		MSAM	39.325	8.090	4.004	7.245	5.743	6.130	**3.280**	3.600
	Case 5	MPSNR	13.363	24.336	33.021	33.710	27.272	28.098	33.763	**34.272**
		MSSIM	0.199	0.731	0.925	0.925	0.835	0.845	0.954	**0.959**
		MSAM	39.320	10.829	4.464	8.521	13.661	14.737	**3.313**	3.747

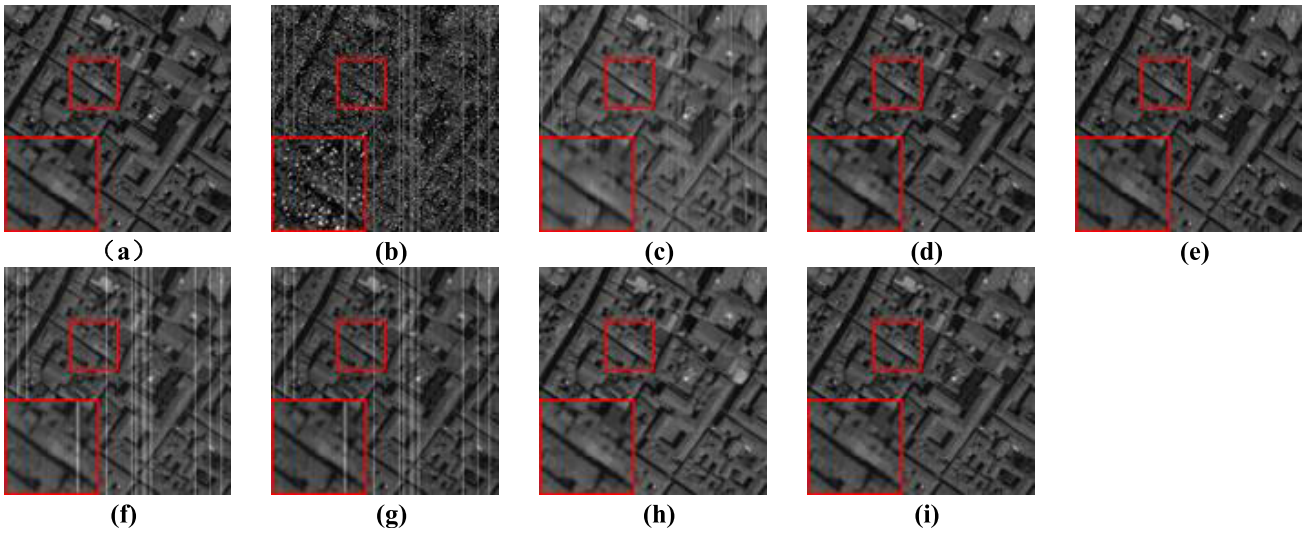

FIGURE 4. Denoising results of Pavia City Center dataset under Case 3. (a) Original. (b) Noisy. (c) NLTR. (d) LRTDTV. (e) LRTDGS. (f) 3DTNN. (g) 3DLogTNN. (h) $FGSLR_{1/2}$. (i) NL3DLogTNN.

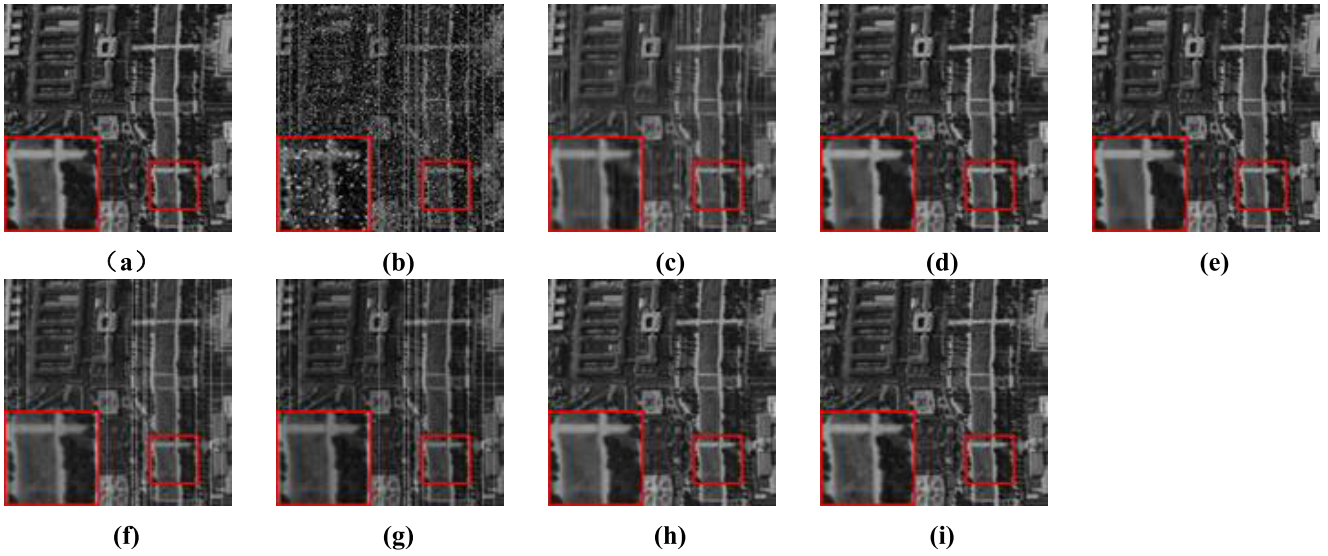

FIGURE 5. Denoising results of Pavia City Center dataset under Case 3. (a) Original. (b) Noisy. (c) NLTR. (d) LRTDTV. (e) LRTDGS. (f) 3DTNN. (g) 3DLogTNN. (h) $FGSLR_{1/2}$. (i) NL3DLogTNN.

both stripe and deadline noise within the visual scope, exhibiting excellent performance in terms of visual quality and detail preservation in the denoised images.

This section discusses the vertical mean profile results obtained from different models on the WHU HongHu dataset, as shown in Figure 8. It should be noted that all the models considered in the comparison have effectively reduced the noise in the original images to some extent. However, except for $FGSLR_{1/2}$ and NL3DLogTNN, other models still exhibit residual noise in their denoised results. In this scenario, the proposed NL3DLogTNN model stands out with remarkable denoising performance, as the line artifacts in the plane profiles are almost eliminated.

Figure 9 shows the visual denoising results for the HYDICE Urban dataset as described in this passage. It is observed that the NLTR, LRTDTV, 3DTNN, and 3DLogTNN models still visually preserve some stripe noise. The proposed method presented in this study demonstrated superior denoising performance and enhance visual quality compared to the other methods. In particular, the proposed model successfully removed all stripe residues from the visual results and preserved more local details, indicating its effectiveness in dealing with complex real-world noise.

Figure 10 illustrates the performance of contrastive models on the HYDICE Urban dataset by analysing their vertical mean profiles, as discussed in this paragraph. It is important

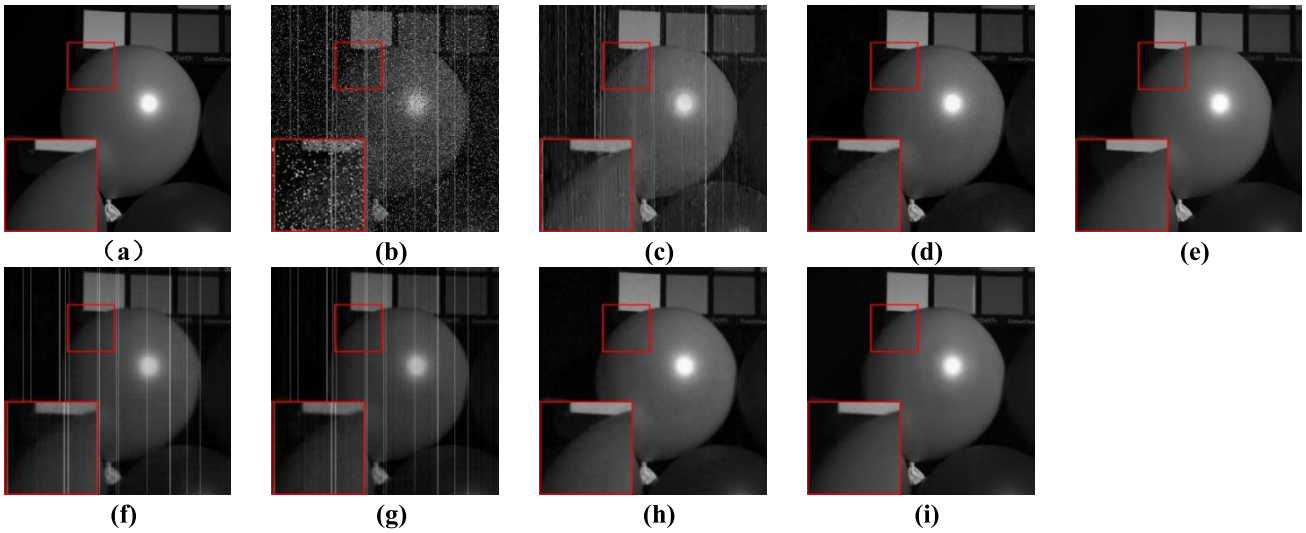

FIGURE 6. Denoising results of the CAVE dataset under Case 3. (a) Original. (b) Noisy. (c) NLTR. (d) LRTDTV. (e) LRTDGS. (f) 3DTNN. (g) 3DLogTNN. (h) FGSLR$_{1/2}$. (i) NL3DLogTNN.

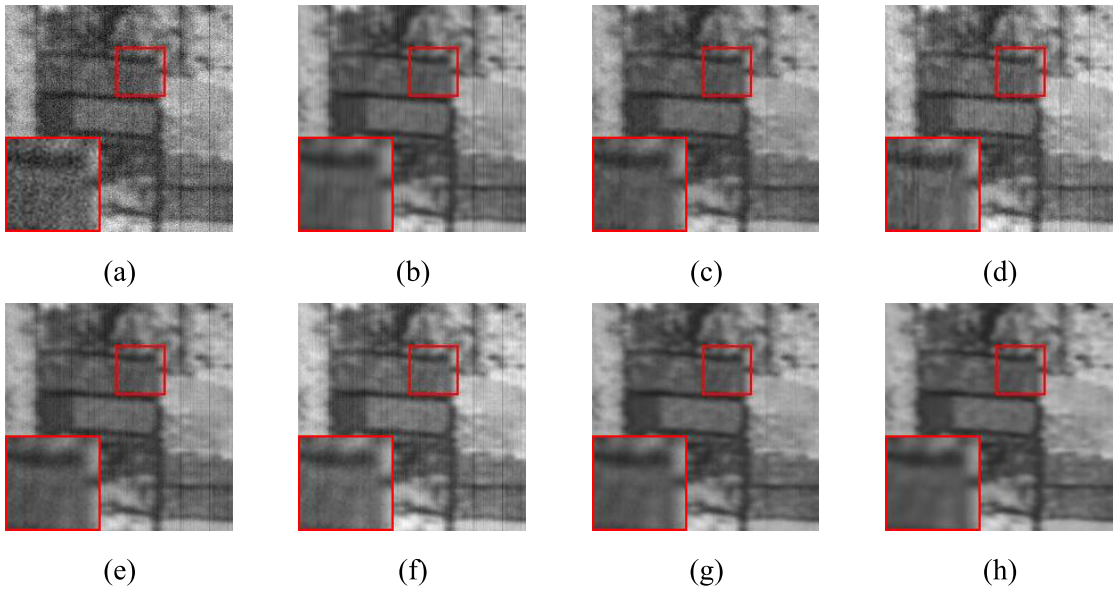

FIGURE 7. Denoising results on the WHU HongHu dataset. (a) Original/Noisy. (b) NLTR. (c) LRTDTV. (d) LRTDGS. (e) 3DTNN. (f) 3DLogTNN. (g) FGSLR$_{1/2}$. (h) NL3DLogTNN.

to note that when compared to the original noisy image, all the models under comparison show some level of noise reduction. However, the NLTR, 3DTNN, and 3DLogTNN models cannot adapt to complex noise and have a large number of residual fluctuations. On the other hand, the proposed model exhibits substantially better denoising performance compared to the other models, almost removing all noise fluctuations, further confirming the effectiveness of combining non-local priors with low-rank tensor decomposition.

C. DISCUSSION

Before running Algorithm 1 for the NL3DLogTNN model, several parameters must be determined, including the patch size P, the number of similar patches K, and the parameter for 3DLogTNN. Although the model includes multiple parameters, they are all highly robust and can be maintained constant across different experiments

1) Analysis of Patch Size P: Figure 11 shows how the MPSNR values vary with the modification of parameter P under contrastive noise levels.

In this study, the denoising performance exhibited by the model proposed is affected by parameter P, and the MPSNR varies considerably with various values of P. Figure 9 shows the MPSNR of the model increases gradually as P increases. When the magnitude of P is less than the range [23], [25], the model achieves its best denoising performance when the

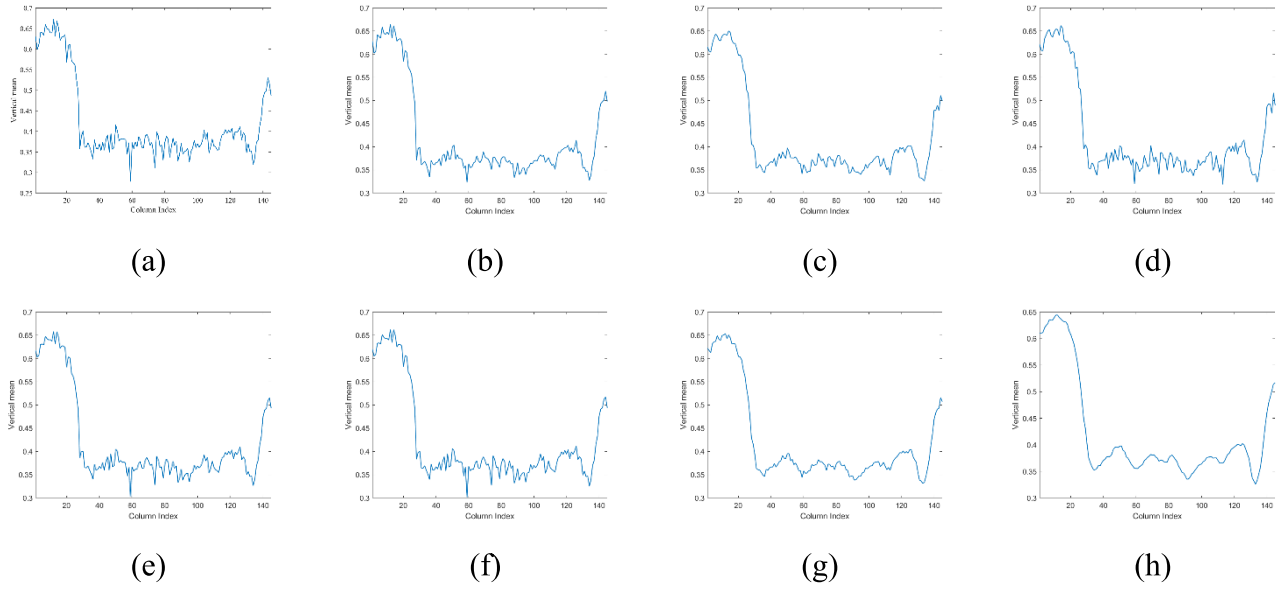

FIGURE 8. The horizontal mean profiles of the WHU HongHu dataset. (a) Original/Noisy. (b) NLTR. (c) LRTDTV. (d) LRTDGS. (e) 3DTNN. (f) 3DLogTNN. (g) $\text{FGSLR}_{881/2}$. (h) NL3DLogTNN.

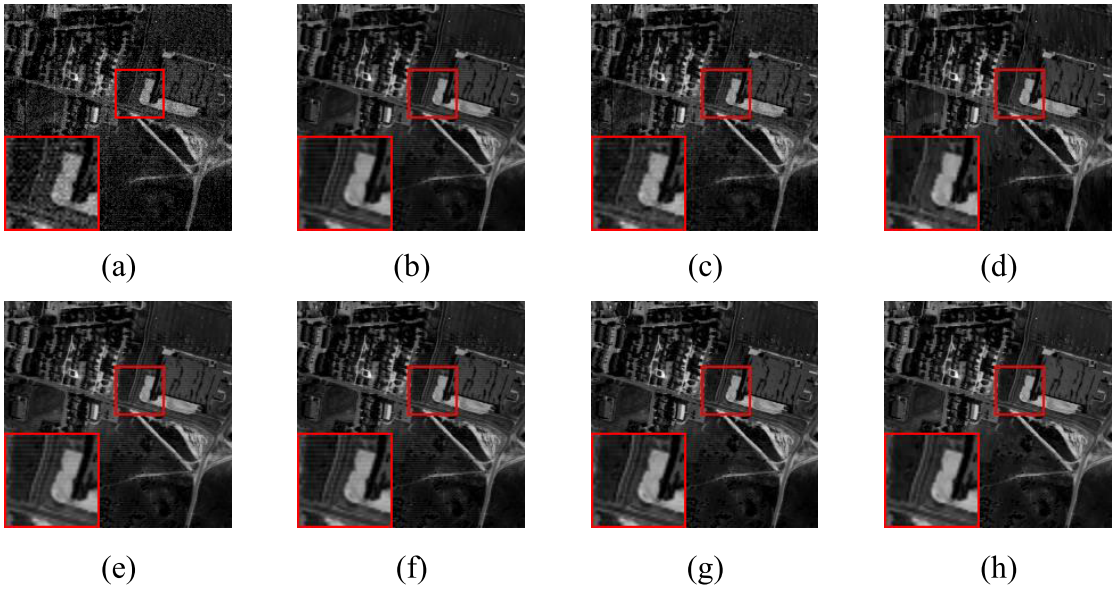

FIGURE 9. The denoising results of the HYDICE Urban dataset. (a) Original/Noisy. (b)NLTR. (c)LRTDTV. (d)LRTDGS. (e)3DTNN. (f)3DLogTNN. (g) $\text{FGSLR}_{1/2}$. (h)NL3DLogTNN.

magnitude of P lies within the interval [23], [25]. However, the model performance began to decline when the numerical parameter P exceeded 25. In this study, considering both the denoising effect and computational cost, P was set to 24 in all experiments.

2) Analysis of the Number of Similar Patches K: Figure 12 shows the correlation between the MPSNR and the number of similar patches K. When the number of non-local similar patches is 200, NL3DLogTNN obtains the highest MPSNR value. Thus, in all the experiments, we set K according to this experience.

3) Analysis of parameter α_k for 3DLogTNN: We examined the stability of the weight parameter in the 3DLogTNN component of the proposed NL3DLogTNN model for Washington DC Mall and Pavia City Center HSIs in various scenarios.

The weight parameter in the proposed NL3DLogTNN method was used to regulate the correlation weights of the individual HSI modes.

According to 3DLogTNN research, the correlation along the spectral mode in the HSI is predicted to be significantly more robust than that along the spatial mode. Furthermore,

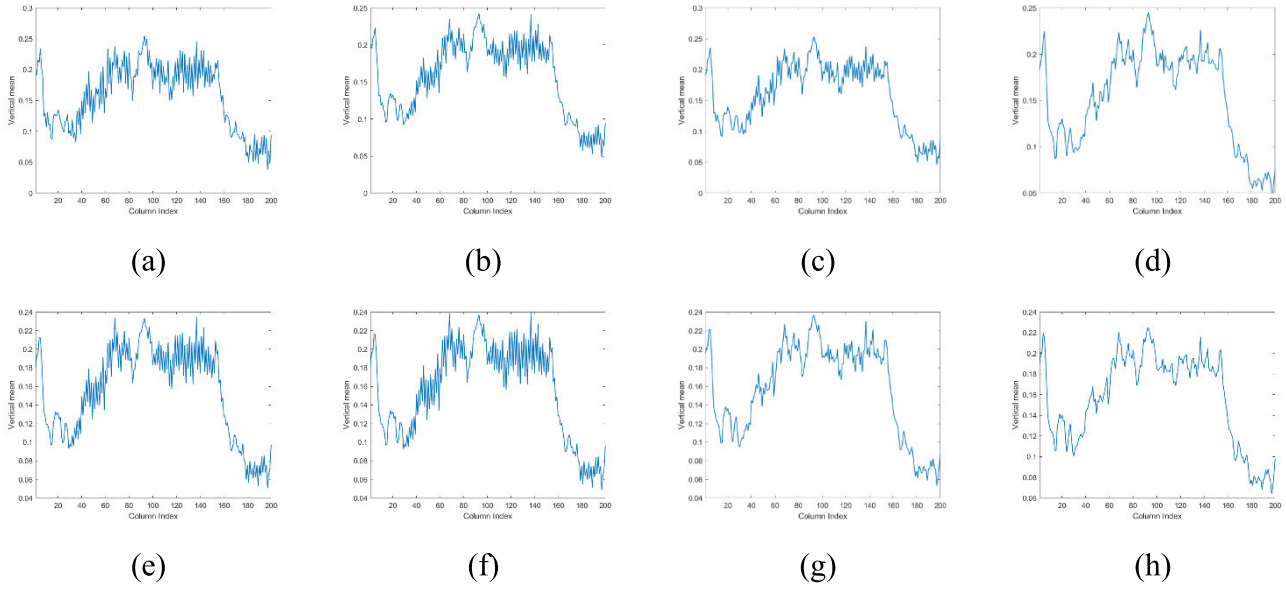

FIGURE 10. The vertical mean profiles of the HYDICE Urban dataset. (a) Original/Noisy. (b) NLTR. (c) LRTDTV. (d) LRTDGS. (e) 3DTNN. (f) 3DLogTNN. (g) FGSLR$_{1/2}$. (h)NL3DLogTNN.

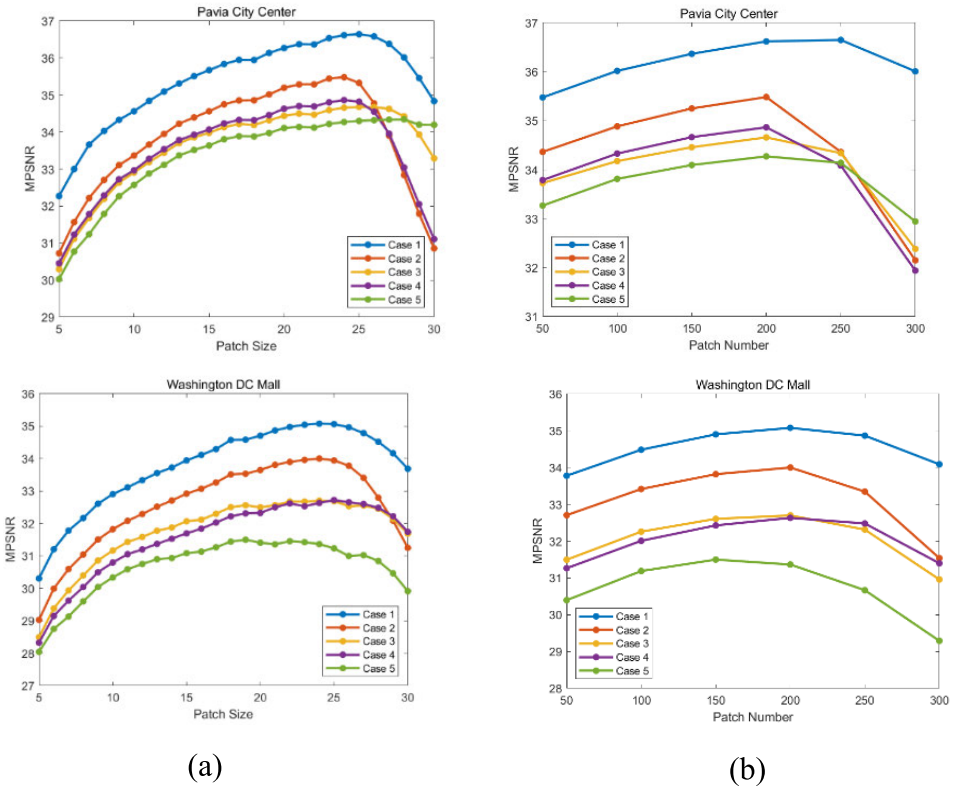

FIGURE 11. Variation of MPSNR values with parameter P at different noise levels.

since KNN is employed in this study for clustering similar patches, the correlation along the third dimension is equal to or stronger than that along the spectral dimension. Thus, we empirically set the weight control parameter θ_2 of the spectral dimension to 1, and select the weight control parameter θ_1 of the similar patch dimension from the range [1,4] and the control parameter θ_3 of the spatial correlation strength from the range [1,0]. We use the MPSNR denoising results

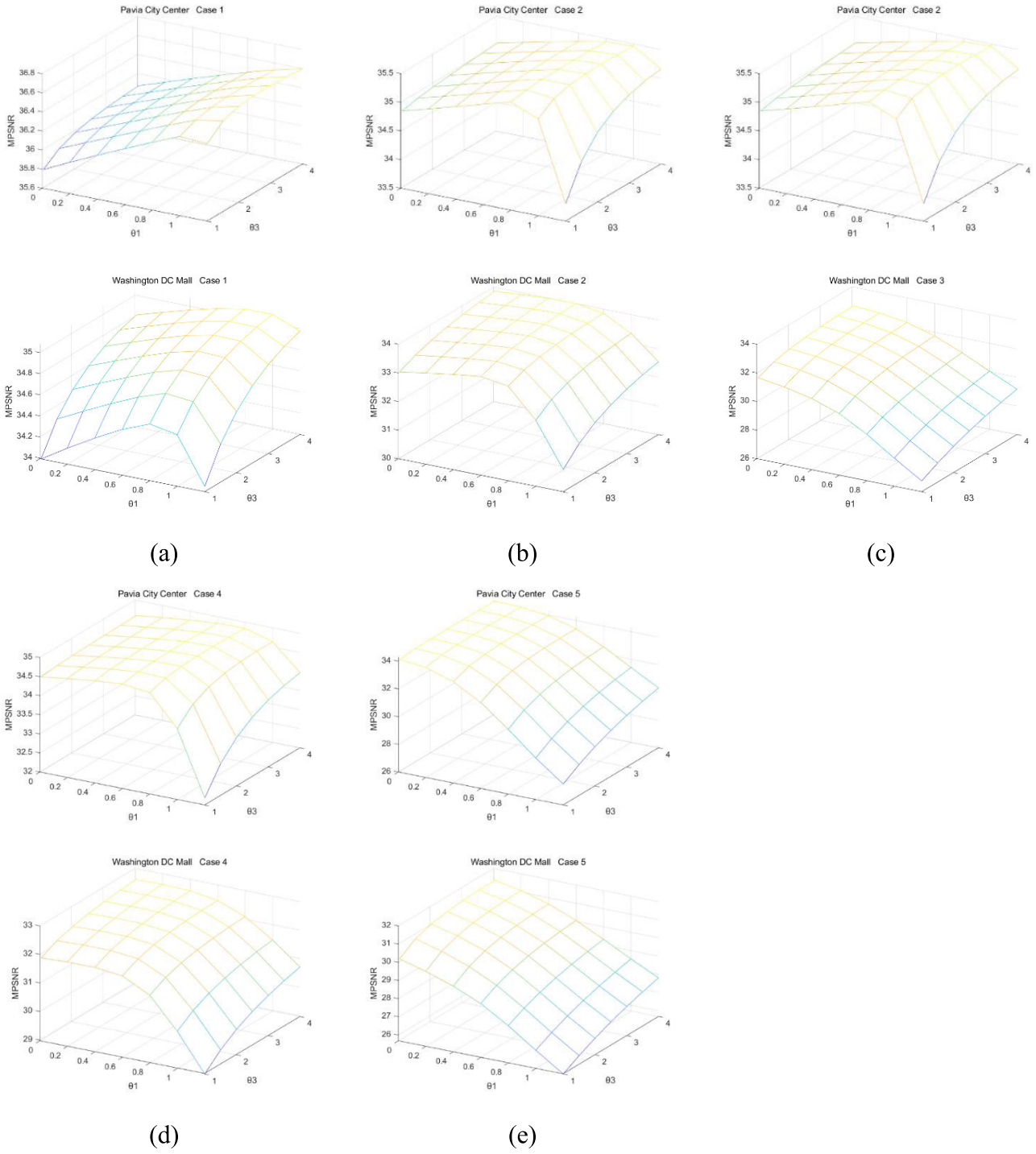

FIGURE 12. The relationship between 3DLogTNN parameters and MPSNR values under various noise levels. (a) Case 1 (b)Case 2 (c) Case 3 (d) Case 4 (e) case5.

as a function of the parameters θ_1 and θ_3, and compute the weight parameter α through $(\theta_1, \theta_2, \theta_3)/(\theta_1 + \theta_2 + \theta_3)$. Figure 12 shows the change of θ_1 is more significant as the noise level increases. When the mixed noise level is highest (i.e. Case 5), θ_1 takes the minimum value because the spatial dimension correlation is the smallest. At the same time, we notice that the variation of θ_3 is relatively stable with the increase in noise level, showing its good robustness and adaptability to noise. Thus, without loss of generality, we simulated and performed experiments on real data with

TABLE 2. Parameters setting in the proposed NL3DLogTNN-BASED HSI denoising methods for simulated data.

Dataset	Case	θ1	θ2
Pavia City Center	Case 1	1.20	2.50
	Case 2	1.00	3.00
	Case 3	0.40	2.50
	Case 4	0.80	3.00
	Case 5	0.01	2.50
Washington DC Mall	Case 1	1.00	4.00
	Case 2	0.60	4.00
	Case 3	0.01	4.00
	Case 4	0.20	4.00
	Case 5	0.01	4.00

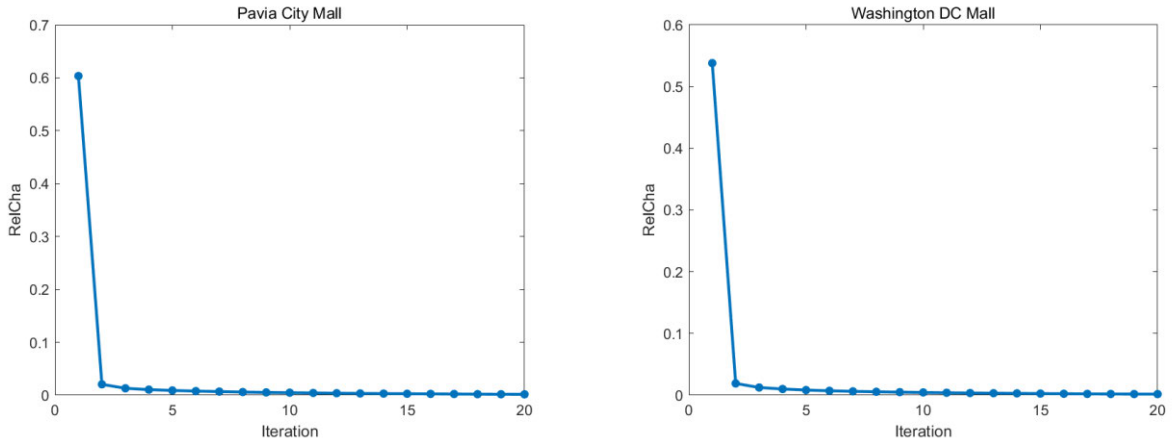

FIGURE 13. Convergence analysis experimental figure.

various values of θ_1 and θ_3 for different noise levels. The values of θ_1 and θ_3 used in the experiments are described as Table 2.

4) Convergence Analysis: First, the NL3DLogTNN algorithm's optimisation objective function demonstrates convexity, which ensures mathematical algorithmic convergence. Additionally, we computed the relative change indicator RelCha to measure the relative change in tensor information between two iterations. Figure 13 shows the RelCha changes of the proposed model for various iteration numbers under the Case 2 scenarios of the Pavia City Mall and Washington DC Mall datasets.

Figure 13 shows that RelCha decreases rapidly in the early stages and gradually reaches stability after three iterations. Therefore, it is feasible to conclude that the NL3DLogTNN model presented in this study demonstrates a rapid convergence within the ADMM framework.

V. CONCLUSION

This study presents a novel method for denoising HSI called NL3DLogTNN that makes use of 3DLogTNN decomposition to exploit the self-similarity and spectral coherence of hyperspectral imagery. To address the proposed NL3DLog TNN decomposition model for HSI denoising, an algorithm based on ADMM was developed. Empirical convergence analysis was also conducted. Comparative experiments were conducted using various state-of-the-art HSI denoising methods on simulated and real datasets, and the results demonstrated the superior denoising performance of the NL3DLogTNN method. Future research may extend the 3DLogTNN denoising platform to other image-processing endeavours. Although the proposed model's noise removal capability is promising, there is still potential for improving the model's performance. Our future study will focus on integrating the NL3DLogTNN model with convolutional neural networks to improve the model's capacity to remove mixed noise, while also decreasing its computational complexity by learning more suitable factor regularisation.

REFERENCES

[1] J. M. Bioucas-Dias, A. Plaza, G. Camps-Valls, P. Scheunders, N. Nasrabadi, and J. Chanussot, "Hyperspectral remote sensing data analysis and future challenges," *IEEE Geosci. Remote Sens. Mag.*, vol. 1, no. 2, pp. 6–36, Jun. 2013, doi: 10.1109/MGRS.2013.2244672.

[2] J. M. Bioucas-Dias, A. Plaza, N. Dobigeon, M. Parente, Q. Du, P. Gader, and J. Chanussot, "Hyperspectral unmixing overview: Geometrical, statistical, and sparse regression-based approaches," *IEEE J. Sel. Topics Appl. Earth Observ. Remote Sens.*, vol. 5, no. 2, pp. 354–379, Apr. 2012, doi: 10.1109/JSTARS.2012.2194696.

[3] P. Ghamisi, N. Yokoya, J. Li, W. Liao, S. Liu, J. Plaza, B. Rasti, and A. Plaza, "Advances in hyperspectral image and signal processing: A comprehensive overview of the state of the art," *IEEE Geosci. Remote Sens. Mag.*, vol. 5, no. 4, pp. 37–78, Dec. 2017, doi: 10.1109/MGRS.2017.2762087.

[4] X.-R. Feng, H.-C. Li, S. Liu, and H. Zhang, "Correntropy-based autoencoder-like NMF with total variation for hyperspectral unmixing," *IEEE Geosci. Remote Sens. Lett.*, vol. 19, pp. 1–5, 2022, doi: 10.1109/LGRS.2020.3020896.

[5] X. Fu, W.-K. Ma, J. M. Bioucas-Dias, and T.-H. Chan, "Semiblind hyperspectral unmixing in the presence of spectral library mismatches," *IEEE Trans. Geosci. Remote Sens.*, vol. 54, no. 9, pp. 5171–5184, Sep. 2016, doi: 10.1109/TGRS.2016.2557340.

[6] F. Xiong, J. Zhou, J. Lu, and Y. Qian, "Nonconvex nonseparable sparse nonnegative matrix factorization for hyperspectral unmixing," *IEEE J. Sel. Topics Appl. Earth Observ. Remote Sens.*, vol. 13, pp. 6088–6100, 2020, doi: 10.1109/JSTARS.2020.3028104.

[7] P. Ghamisi, J. Plaza, Y. Chen, J. Li, and A. J. Plaza, "Advanced spectral classifiers for hyperspectral images: A review," *IEEE Geosci. Remote Sens. Mag.*, vol. 5, no. 1, pp. 8–32, Mar. 2017, doi: 10.1109/MGRS.2016.2616418.

[8] B. Rasti, P. Scheunders, P. Ghamisi, G. Licciardi, and J. Chanussot, "Noise reduction in hyperspectral imagery: Overview and application," *Remote Sens.*, vol. 10, no. 3, p. 482, Mar. 2018, doi: 10.3390/rs10030482.

[9] S. Prasad, D. Labate, M. Cui, and Y. Zhang, "Morphologically decoupled structured sparsity for rotation-invariant hyperspectral image analysis," *IEEE Trans. Geosci. Remote Sens.*, vol. 55, no. 8, pp. 4355–4366, Aug. 2017, doi: 10.1109/TGRS.2017.2691607.

[10] N. Yokoya, C. Grohnfeldt, and J. Chanussot, "Hyperspectral and multispectral data fusion: A comparative review of the recent literature," *IEEE Geosci. Remote Sens. Mag.*, vol. 5, no. 2, pp. 29–56, Jun. 2017, doi: 10.1109/MGRS.2016.2637824.

[11] J. Li, X. Liu, Q. Yuan, H. Shen, and L. Zhang, "Antinoise hyperspectral image fusion by mining tensor low-multilinear-rank and variational properties," *IEEE Trans. Geosci. Remote Sens.*, vol. 57, no. 10, pp. 7832–7848, Oct. 2019, doi: 10.1109/TGRS.2019.2916654.

[12] H. Fan, J. Li, Q. Yuan, X. Liu, and M. Ng, "Hyperspectral image denoising with bilinear low rank matrix factorization," *Signal Process.*, vol. 163, pp. 132–152, Oct. 2019, doi: 10.1016/j.sigpro.2019.04.029.

[13] J. Yang, Y.-Q. Zhao, J. C. Chan, and S. G. Kong, "Coupled sparse denoising and unmixing with low-rank constraint for hyperspectral image," *IEEE Trans. Geosci. Remote Sens.*, vol. 54, no. 3, pp. 1818–1833, Mar. 2016, doi: 10.1109/TGRS.2015.2489218.

[14] H. Zhang, W. He, L. Zhang, H. Shen, and Q. Yuan, "Hyperspectral image restoration using low-rank matrix recovery," *IEEE Trans. Geosci. Remote Sens.*, vol. 52, no. 8, pp. 4729–4743, Aug. 2014, doi: 10.1109/TGRS.2013.2284280.

[15] J. Lin, T.-Z. Huang, X.-L. Zhao, T.-X. Jiang, and L. Zhuang, "A tensor subspace representation-based method for hyperspectral image denoising," *IEEE Trans. Geosci. Remote Sens.*, vol. 59, no. 9, pp. 7739–7757, Sep. 2021, doi: 10.1109/TGRS.2020.3032168.

[16] W. He, H. Zhang, L. Zhang, and H. Shen, "Total-variation-regularized low-rank matrix factorization for hyperspectral image restoration," *IEEE Trans. Geosci. Remote Sens.*, vol. 54, no. 1, pp. 178–188, Jan. 2016, doi: 10.1109/TGRS.2015.2452812.

[17] N. Renard, S. Bourennane, and J. Blanc-Talon, "Denoising and dimensionality reduction using multilinear tools for hyperspectral images," *IEEE Geosci. Remote Sens. Lett.*, vol. 5, no. 2, pp. 138–142, Apr. 2008, doi: 10.1109/LGRS.2008.915736.

[18] Y. Chen, W. He, N. Yokoya, and T.-Z. Huang, "Hyperspectral image restoration using weighted group sparsity-regularized low-rank tensor decomposition," *IEEE Trans. Cybern.*, vol. 50, no. 8, pp. 3556–3570, Aug. 2020, doi: 10.1109/TCYB.2019.2936042.

[19] X. Bai, F. Xu, L. Zhou, Y. Xing, L. Bai, and J. Zhou, "Nonlocal similarity based nonnegative tucker decomposition for hyperspectral image denoising," *IEEE J. Sel. Topics Appl. Earth Observ. Remote Sens.*, vol. 11, no. 3, pp. 701–712, Mar. 2018, doi: 10.1109/JSTARS.2018.2791718.

[20] Y. Wang, J. Peng, Q. Zhao, Y. Leung, X.-L. Zhao, and D. Meng, "Hyperspectral image restoration via total variation regularized low-rank tensor decomposition," *IEEE J. Sel. Topics Appl. Earth Observ. Remote Sens.*, vol. 11, no. 4, pp. 1227–1243, Apr. 2018, doi: 10.1109/JSTARS.2017.2779539.

[21] Y. Chen, T.-Z. Huang, and X.-L. Zhao, "Destriping of multispectral remote sensing image using low-rank tensor decomposition," *IEEE J. Sel. Topics Appl. Earth Observ. Remote Sens.*, vol. 11, no. 12, pp. 4950–4967, Dec. 2018, doi: 10.1109/JSTARS.2018.2877722.

[22] X. Liu, S. Bourennane, and C. Fossati, "Denoising of hyperspectral images using the PARAFAC model and statistical performance analysis," *IEEE Trans. Geosci. Remote Sens.*, vol. 50, no. 10, pp. 3717–3724, Oct. 2012, doi: 10.1109/TGRS.2012.2187063.

[23] Z. Zhang, G. Ely, S. Aeron, N. Hao, and M. Kilmer, "Novel methods for multilinear data completion and de-noising based on tensor-SVD," in *Proc. IEEE Conf. Comput. Vis. Pattern Recognit.*, Columbus, OH, USA, Jun. 2014, pp. 3842–3849, doi: 10.1109/CVPR.2014.485.

[24] Z. Zhang and S. Aeron, "Exact tensor completion using t-SVD," *IEEE Trans. Signal Process.*, vol. 65, no. 6, pp. 1511–1526, Mar. 2017, doi: 10.1109/TSP.2016.2639466.

[25] C. Lu, J. Feng, Y. Chen, W. Liu, Z. Lin, and S. Yan, "Tensor robust principal component analysis: Exact recovery of corrupted low-rank tensors via convex optimization," in *Proc. IEEE Conf. Comput. Vis. Pattern Recognit. (CVPR)*, Jun. 2016, pp. 5249–5257, doi: 10.1109/CVPR.2016.567.

[26] Y.-B. Zheng, T.-Z. Huang, X.-L. Zhao, T.-X. Jiang, T.-Y. Ji, and T.-H. Ma, "Tensor N-tubal rank and its convex relaxation for low-rank tensor recovery," *Inf. Sci.*, vol. 532, pp. 170–189, Sep. 2020, doi: 10.1016/j.ins.2020.05.005.

[27] H. Fan, Y. Chen, Y. Guo, H. Zhang, and G. Kuang, "Hyperspectral image restoration using low-rank tensor recovery," *IEEE J. Sel. Topics Appl. Earth Observ. Remote Sens.*, vol. 10, no. 10, pp. 4589–4604, Oct. 2017, doi: 10.1109/JSTARS.2017.2714338.

[28] Y. Peng, D. Meng, Z. Xu, C. Gao, Y. Yang, and B. Zhang, "Decomposable nonlocal tensor dictionary learning for multispectral image denoising," in *Proc. IEEE Conf. Comput. Vis. Pattern Recognit.*, Columbus, OH, USA, Jun. 2014, pp. 2949–2956, doi: 10.1109/CVPR.2014.377.

[29] Q. Xie, Q. Zhao, D. Meng, Z. Xu, S. Gu, W. Zuo, and L. Zhang, "Multispectral images denoising by intrinsic tensor sparsity regularization," in *Proc. IEEE Conf. Comput. Vis. Pattern Recognit. (CVPR)*, Las Vegas, NV, USA, Jun. 2016, pp. 1692–1700, doi: 10.1109/CVPR.2016.187.

[30] Y. Chang, L. Yan, and S. Zhong, "Hyper-Laplacian regularized unidirectional low-rank tensor recovery for multispectral image denoising," in *Proc. IEEE Conf. Comput. Vis. Pattern Recognit. (CVPR)*, Honolulu, HI, USA, Jul. 2017, pp. 5901–5909, doi: 10.1109/CVPR.2017.625.

[31] W. He, Q. Yao, C. Li, N. Yokoya, and Q. Zhao, "Non-local meets global: An integrated paradigm for hyperspectral denoising," in *Proc. IEEE/CVF Conf. Comput. Vis. Pattern Recognit. (CVPR)*, Long Beach, CA, USA, Jun. 2019, pp. 6861–6870, doi: 10.1109/CVPR.2019.00703.

[32] Q. Xie, Q. Zhao, D. Meng, and Z. Xu, "Kronecker-Basis-Representation based tensor sparsity and its applications to tensor recovery," *IEEE Trans. Pattern Anal. Mach. Intell.*, vol. 40, no. 8, pp. 1888–1902, Aug. 2018, doi: 10.1109/TPAMI.2017.2734888.

[33] J. Xue, Y. Zhao, W. Liao, and S. G. Kong, "Joint spatial and spectral low-rank regularization for hyperspectral image denoising," *IEEE Trans. Geosci. Remote Sens.*, vol. 56, no. 4, pp. 1940–1958, Apr. 2018, doi: 10.1109/TGRS.2017.2771155.

[34] M. Maggioni, V. Katkovnik, K. Egiazarian, and A. Foi, "Nonlocal transform-domain filter for volumetric data denoising and reconstruction," *IEEE Trans. Image Process.*, vol. 22, no. 1, pp. 119–133, Jan. 2013, doi: 10.1109/TIP.2012.2210725.

[35] A. Danielyan, A. Foi, V. Katkovnik, and K. Egiazarian, "Denoising of multispectral images via nonlocal groupwise spectrum-PCA," in *Proc. Conf. Colour Graph., Imag., Vis.*, 2010, vol. 5, no. 1, pp. 261–266, doi: 10.2352/CGIV.2010.5.1.art00042.

[36] Y. Chen, W. He, N. Yokoya, T.-Z. Huang, and X.-L. Zhao, "Nonlocal tensor-ring decomposition for hyperspectral image denoising," *IEEE Trans. Geosci. Remote Sens.*, vol. 58, no. 2, pp. 1348–1362, Feb. 2020, doi: 10.1109/TGRS.2019.2946050.

[37] Y. Chang, L. Yan, X.-L. Zhao, H. Fang, Z. Zhang, and S. Zhong, "Weighted low-rank tensor recovery for hyperspectral image restoration," *IEEE Trans. Cybern.*, vol. 50, no. 11, pp. 4558–4572, Nov. 2020, doi: 10.1109/TCYB.2020.2983102.

[38] Y. Chang, L. Yan, H. Fang, S. Zhong, and W. Liao, "HSI-DeNet: Hyperspectral image restoration via convolutional neural network," *IEEE Trans. Geosci. Remote Sens.*, vol. 57, no. 2, pp. 667–682, Feb. 2019.
[39] J. Xue, Y. Zhao, S. Huang, W. Liao, J. C. Chan, and S. G. Kong, "Multilayer sparsity-based tensor decomposition for low-rank tensor completion," *IEEE Trans. Neural Netw. Learn. Syst.*, vol. 33, no. 11, pp. 6916–6930, Nov. 2022, doi: 10.1109/TNNLS.2021.3083931.
[40] H. Zeng, J. Xue, H. Q. Luong, and W. Philips, "Multimodal core tensor factorization and its applications to low-rank tensor completion," *IEEE Trans. Multimedia*, early access, Oct. 25, 2022, doi: 10.1109/TMM.2022.3216746.
[41] H. Liu, J. Zhang, and R. Xiong, "CAS: Correlation adaptive sparse modeling for image denoising," *IEEE Trans. Comput. Imag.*, vol. 7, pp. 638–647, 2021, doi: 10.1109/TCI.2021.3083135.
[42] Y. Chang, L. Yan, B. Chen, S. Zhong, and Y. Tian, "Hyperspectral image restoration: Where does the low-rank property exist," *IEEE Trans. Geosci. Remote Sens.*, vol. 59, no. 8, pp. 6869–6884, Aug. 2021, doi: 10.1109/TGRS.2020.3024623.
[43] Q. Yuan, Q. Zhang, J. Li, H. Shen, and L. Zhang, "Hyperspectral image denoising employing a spatial–spectral deep residual convolutional neural network," *IEEE Trans. Geosci. Remote Sens.*, vol. 57, no. 2, pp. 1205–1218, Feb. 2019, doi: 10.1109/TGRS.2018.2865197.
[44] K. Wei, Y. Fu, and H. Huang, "3-D quasi-recurrent neural network for hyperspectral image denoising," *IEEE Trans. Neural Netw. Learn. Syst.*, vol. 32, no. 1, pp. 363–375, Jan. 2021, doi: 10.1109/TNNLS.2020.2978756.
[45] Y. Chen, T.-Z. Huang, W. He, X.-L. Zhao, H. Zhang, and J. Zeng, "Hyperspectral image denoising using factor group sparsity-regularized nonconvex low-rank approximation," *IEEE Trans. Geosci. Remote Sens.*, vol. 60, 2022, Art. no. 5515916.

HAORAN LIU is currently pursuing the degree in intelligent manufacturing engineering with the Shandong University of Science and Technology (SDUST), Qingdao, China. Her current research interests include tensor decomposition, artificial intelligence, and machine vision.

TIANYU SU is currently pursuing the degree in the Internet of Things (IoT) with the Shandong University of Science and Technology (SDUST). His current research interests include neural networks and algorithms of computer vision.

XINZHE DU is currently pursuing the degree in automation with the Shandong University of Science and Technology, Qingdao, China. His current research interests include pattern recognition and intelligent systems.

YUXIN ZHAI is currently pursuing the degree in transportation with the Shandong University of Science and Technology of China (SDUST), Qingdao, China. Her current research interests include vehicle-road collaboration, vehicle networking and traffic big data, and models and algorithms for video image processing.

JIANLI ZHAO received the Ph.D. degree from the Department of Computer Application Technology, Northeastern University, China, in 2006. He is currently the Associate Dean of the School of Computer Science and Engineering, Shandong University of Science and Technology, and the Secretary-General of the Qingdao Branch, China Computer Federation. His current research interests include traffic big data analysis, personalized recommendation algorithms, and behaviour computation.